

# ON THE USE OF 3D IMAGES AND 3D DISPLACEMENT MEASUREMENTS FOR THE ANALYSIS OF DAMAGE MECHANISMS IN CONCRETE-LIKE MATERIALS

FRANCOIS HILD\*, STEPHANE ROUX\*, DOMINIQUE BERNARD<sup>‡</sup>, GREGORY HAUSS<sup>‡</sup>  
AND MEHDI REBAI<sup>‡</sup>

\*Laboratoire de Mécanique et Technologie (LMT-Cachan)  
ENS Cachan / CNRS / UPMC / PRES UniverSud Paris  
61 avenue du Président Wilson, F-94235 Cachan Cedex, France  
e-mail: {firstname.lastname}@lmt.ens-cachan.fr

<sup>‡</sup>CNRS, ICMCB, UPR 9048, F-33600 Pessac, France  
Univ. Bordeaux, ICMCB, UPR 9048, F-33600 Pessac, France  
e-mail: {lastname}@icmcb-bordeaux.cnrs.fr

**Key words:** Correlation residuals, damage mechanism, digital volume correlation, displacement and strain resolutions, X-ray microtomography.

**Abstract.** A three dimensional analysis of a drying test on a concrete-like material is presented. The analysis combines different tools, namely, X-ray microtomography of an *ex situ* experiment, image acquisition and processing, volume correlation to measure three dimensional displacement fields. It allows in particular mesoscopic strain analyses to be performed. By studying the correlation residuals, it is also possible to study the damage mechanisms.

## 1 INTRODUCTION

The invaluable information provided by tomography in the field of material science has been essentially focused on 3D imaging, and hence, with the help of 3D image analysis techniques, access to the constitutive phases of a material, their morphology, the statistical characterization of inclusion number, size, shape has received a lot of attention, and indeed, this effort has revealed very rewarding [1, 2]. A second very appealing virtue of tomography in the industrial context is shape metrology [3]. This pushed tomography to become even more quantitative than what was called for in simple imaging. It is now very tempting to follow the evolution of a specimen during its mechanical loading, and hence *in situ* mechanical testing is an expanding field of investigation [4]. To get ad-

ditional information from these tests, one technique of predilection to measure 3D displacement fields is Digital Volume Correlation.

To study cement and concrete at the microscale, microtomography has been used over the last two decades. 3D imaging has been applied to study microstructural features (*e.g.*, porosity [5] or aggregate [6, 7] distributions, aggregate shapes [8], connectivity and tortuosity [9, 10]). Various phenomena such as the alkali-silica reaction [11, 12], microstructural changes and damage during cement hydration [13], damage induced by leaching in mortar [14, 15] or sulfate attack [16, 17] have also been studied. By resorting to *in situ* [5] or *ex situ* [18] mechanical tests it was also possible to analyze the development of damage in these materials. However, there are very few studies, if any, dealing with kinematic measurements

applied to cement and concrete microstructures. One of the challenges is related to the very small levels of strain. The aim of the following analyses is to show that displacement fields can be measured even under these very difficult circumstances.

Digital Volume Correlation (DVC) allows 3D displacement fields to be measured from 3D images acquired, for instance, with X-ray Computed Tomography (X-CT) systems. DVC is a straightforward extension of Digital Image Correlation (DIC [19]) in three dimensions and thus the different strategies developed in 2D are transposed in 3D with comparable weaknesses or merits [19, 20]. In the same way as DIC is progressively being used routinely in solid mechanics, it is a safe bet to predict a similar development in the forthcoming decade as (lab) tomographs will become more common instruments. Furthermore, it is possible to couple experiments with numerical simulations for, say, identification and validation purposes thanks to measured displacement fields in the bulk [21].

In the following, a Galerkin approach to DVC [22] is used to measure displacement and evaluate strain fields during a drying test on a concrete-like cylinder. In Section 2, the studied material, the experimental configuration and the imaging system are presented. The correlation algorithm used herein is briefly recalled in Section 3 and its *a priori* performance is evaluated by artificially adding noise to a reference volume. This type of analysis enables for the evaluation of measurement uncertainties in terms of strains. The experimental results are finally analyzed in Section 4 where displacement and strain fields, and correlation residuals are considered. The latter ones are used to assess the damage mechanism and state of the studied material.

## 2 EXPERIMENT

The cementitious composite considered in this study is made of 35 vol.% of glass beads (diameter equal to 2 mm) included in a cement paste (cement CEM II/B 32,5R; water/cement ratio equal to 0.5). The scanned sample is

a cylinder (8-mm in diameter, and 20-mm in height) cored from a larger sample (parallelepiped  $40 \times 40 \times 160 \text{ mm}^3$  in volume cured in water at  $20 \text{ }^\circ\text{C}$  for 6 months). After coring and before the initial scan, the sample was preserved from desiccation. Then the sample was dried during 23 hours at  $60 \text{ }^\circ\text{C}$  and scanned again. The last step consists of 4 hours at  $60 \text{ }^\circ\text{C}$  followed by 20 hours at  $105 \text{ }^\circ\text{C}$ , and a last scan.

Microtomographic acquisitions were performed on the beam line BM05 of the European Synchrotron Radiation Facility (ESRF, Grenoble, France) using a monochromatic beam with energy of 30 keV. 900 radiographs were acquired at equally spaced angles between  $0^\circ$  and  $180^\circ$  using the FRELON CCD camera. The resulting  $2048 \times 2048$ -pixel radiographs were used to reconstruct, via the conventional filtered back-projection algorithm, 3D images having cubic voxels of volume  $5.1 \times 5.1 \times 5.1 \text{ }\mu\text{m}^3$ .

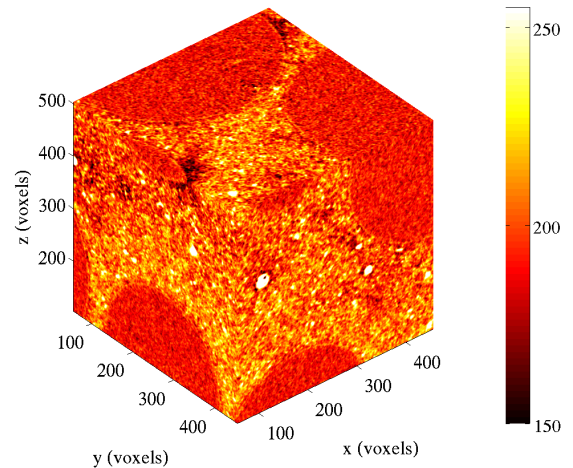


Figure 1:  $400 \times 400 \times 400$ -voxel volume of interest (8-bit digitization) of the analyzed sample in its reference configuration

The analyzed volume of interest (VOI) is shown in Figure 1 where the 2-mm inclusions can be observed. The corresponding gray level histogram is given in Figure 2. The texture is rather poor as only a small part of the 256 gray levels is used and one of the challenges will be to correlate this information to measure displacement fields. This choice was dictated by the fact that in other parts of the reconstructed

volume porosities (with very small gray levels) are more numerous.

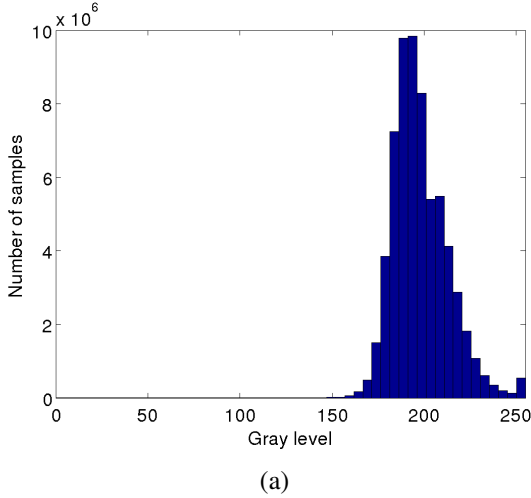


Figure 2: Gray level histogram of the volume shown in Figure 1

### 3 DIGITAL VOLUME CORRELATION

In this section, the correlation algorithm is first presented. Its performance is evaluated by using an *a priori* resolution analysis whereby a reference volume is considered, noise is added to it to form a new volume, and the strain resolution is evaluated by correlating these two volumes.

#### 3.1 Galerkin approach to DVC

DVC consists in registering the texture of two volumes, namely a first one  $f$  in the reference configuration, and another one  $g$  in the deformed configuration. To estimate the unknown displacement field  $\mathbf{u}(\mathbf{x})$ , the squared difference  $\varphi^2(\mathbf{x}) = [f(\mathbf{x}) - g(\mathbf{x} + \mathbf{u}(\mathbf{x}))]^2$  is integrated over the volume of interest  $\Omega$

$$\Phi^2 = \int_{\Omega} \varphi^2(\mathbf{x}) \, d\mathbf{x} \quad (1)$$

and minimized with respect to the degrees of freedom  $a_i$  of the measured displacement field

$$\mathbf{u}(\mathbf{x}) = \sum_i a_i \mathbf{N}_i(\mathbf{x}) \quad (2)$$

where  $\mathbf{N}_i(\mathbf{x})$  are the components of the chosen kinematic basis. In the present case, a 3D finite element kinematics is chosen for the sought

fields, so that  $\mathbf{N}_i$  correspond to the shape functions, here trilinear polynomials associated with 8-node cube elements (or C8-DVC [22]). This approach is referred to as global since the displacement field is evaluated over the whole VOI by globally minimizing  $\Phi^2$ . Other approaches can be found, namely, as in 2D applications [19, 20], the most commonly used correlation algorithms consist in independent registration of small zones of interest to determine mean displacement components [19]. The same type of hypotheses are made in three-dimensional algorithms [23–26]. The latter ones are referred to as local.

To assess the quality of a correlation result, the *correlation residuals* are the only data available when the measured displacements are unknown. In the following, the normalized correlation residual is considered

$$\eta(\mathbf{x}) = \frac{|\varphi(\mathbf{x})|}{\max_{\Omega}(f) - \min_{\Omega}(f)} \quad (3)$$

and its mean value  $\langle \eta \rangle$  is computed over the whole VOI  $\Omega$ .

One key aspect of correlation analyses is the choice of the element size. In the present case, uniform meshes made of C8 elements are considered. The element size  $\ell$  refers to the length of any edge of C8 cubes. The fact that the minimization of the correlation residuals is an ill-posed problem will lead to a compromise between measurement uncertainties and element size, as will be exemplified in the following resolution analysis.

#### 3.2 Resolution analysis

Before studying the displacement field between two actual (*i.e.*, reconstructed) volumes, it is important to evaluate the level of uncertainty attached to both the natural texture of the image and the algorithm used. To assess the resolution, a white Gaussian noise is added to the reference volume (Figure 1) to form the volume in the deformed configuration. Standard deviations of  $2\sqrt{2}$  and  $6\sqrt{2}$  gray levels are considered for the simulated noise. The  $\sqrt{2}$  factor is related to the fact that the noise is only as-

signed to  $g$ , and is therefore representative of the level associated with the volume difference  $f - g$ , namely, twice the variance of noise associated with  $f$  or  $g$  [20]. The correlation procedure is then run blindly on this pair of volumes. The mean initial correlation residual (*i.e.*, the raw picture difference) is equal to 0.88 % of the dynamic range in the first case, and 2.64 % in the second case (*i.e.*, three times higher). It is as expected proportional to the noise level. At convergence, the level of  $\langle \eta \rangle$  is very close for large element sizes. For 12-voxel elements, and the first noise level, the mean normalized residual is equal to 0.86 %, *i.e.*, virtually identical to the initial value. However, for the second noise level, the mean normalized residual is equal to 2.15 %, *i.e.*, lower than the initial value. This reduction is not necessarily a good result because it indicates that with the present texture, the correlation algorithm becomes sensitive to noise for small element sizes.

The mean strains per element are computed from the mean displacement gradient. It was checked that the mean values were less than the corresponding standard deviations. Only the latter ones are reported hereafter. Figure 3 shows the change of the standard strain resolution  $\sigma_\epsilon$  as a function of the element size  $\ell$ . It can be shown [20, 27] that  $\sigma_\epsilon$  varies with  $\ell$  as

$$\sigma_\epsilon \approx B^{5/2} \ell^{-5/2} \quad (4)$$

where  $B$  is a constant of the order of 1 voxel (in the present case  $B = 0.9$  voxel for a standard deviation of  $2\sqrt{2}$  gray levels, and  $B = 1.4$  voxel for a standard deviation of  $6\sqrt{2}$  gray levels), which depends upon the analyzed texture and the interpolation functions used in the DVC analysis [28]. The power  $-5/2$  describes accurately the variation of the strain resolution with the element size for small element sizes. For large element sizes, it departs from the previous interpolation because the resolution associated with nodes belonging to the external boundary of the VOI have higher resolutions [20].

Figure 3 also shows the strain resolution is on average 2.9 times higher for the second noise

level as compared to the first one (*i.e.*, with a standard deviation three times lower than the former).

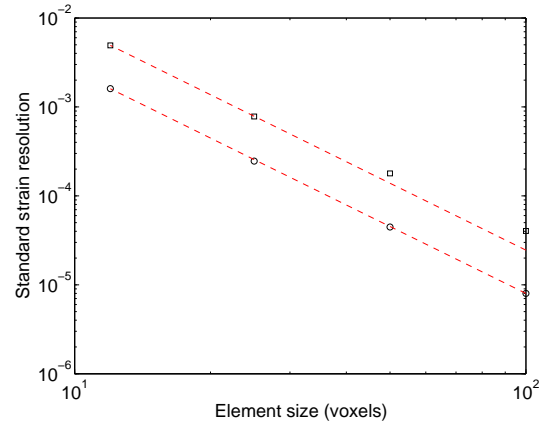


Figure 3: Standard strain resolution  $\sigma_\epsilon$  as a function of the element size  $\ell$  when only inner nodes are considered. The circles correspond to a white noise with a standard deviation of  $2\sqrt{2}$  gray levels, and the squares to a standard deviation of  $6\sqrt{2}$  gray levels. The dashed lines correspond to the power law described by Equation (4)

## 4 ANALYSIS OF THE RESULTS

### 4.1 Correlation residuals

The correlation residuals are used to make sure that the registration was successful [22, 30, 31]. Figure 4 shows three 3D renderings of correlation residuals when the first step is analyzed. The first residual corresponds to the initial volume difference when no corrections are made (Figure 4(a)). An element size of 50 voxels has been used. There is a clear mismatch between the two analyzed states, and the microstructure is clearly visible. The corresponding value of  $\langle \eta \rangle$  is equal to 6.0 %. When an initial correction estimated as a rigid body translation is performed, it leads to the second residual that shows the effect of this first correction (Figure 4(b)). However, there are still zones in which the residuals are high and microstructural features are still observable. The value of  $\langle \eta \rangle$  decreases to 4.3 %.

Last, the third map shows the residuals at convergence (Figure 4(c)). Except for cracked areas, the residuals are low everywhere else.

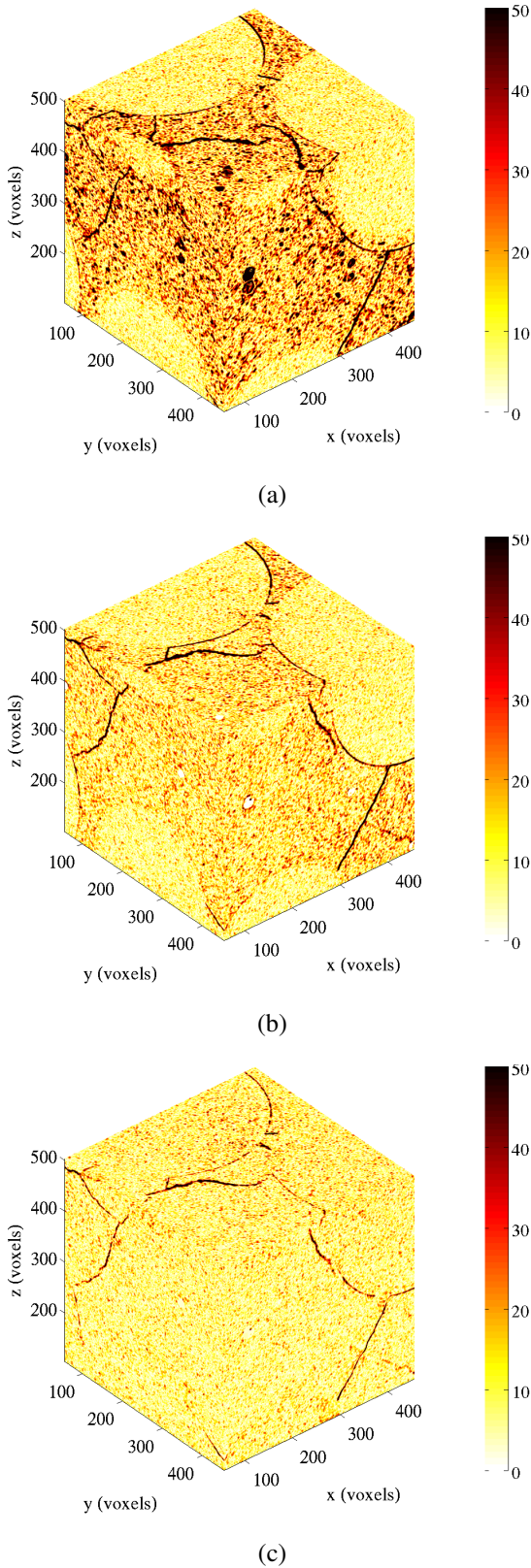


Figure 4: Initial (a), with rigid body translation correction (b), and at convergence (c) gray level residuals  $|f-g|$  when the volume  $g$  of the first load level is registered with the reference volume  $f$  ( $\ell = 50$  voxels)

This result is due to the fact that the chosen kinematics does not allow for displacement discontinuities. Therefore, the correlation residuals enable the discontinuity zones to be located. For these last residuals, it is impossible to locate inclusions and matrix. This is a final evidence that the registration is trustworthy.

This result is confirmed when the shape and range of the histogram of correlation residuals  $|\varphi|$  at convergence (Figure 5) are compared with those of the initial texture (Figure 2). The latter is monomodal and is essentially concentrated around small gray levels as opposed to the former that essentially ranges from 150 to 255 gray levels. A first part of the residual distribution is due to noise associated with the acquisition and reconstruction steps of computed tomography, and the second part to the presence of cracks.

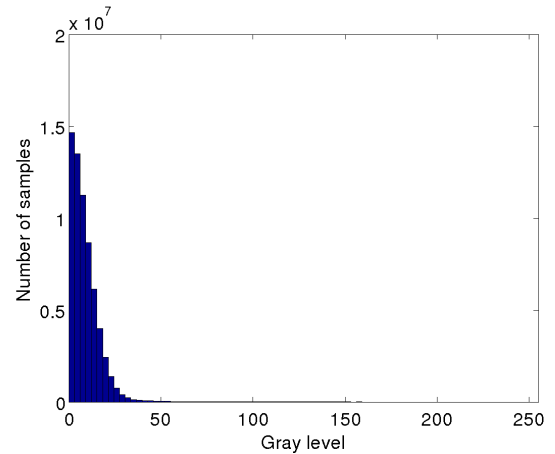


Figure 5: Gray level histogram of the residuals  $|f-g|$  at convergence (Figure 4(c)) to be compared with that shown in Figure 2 when 50-voxel elements are considered

When the element size changes, so does the kinematic basis and the mean correlation residual at convergence. The latter is equal to 3.2 % for 12-voxel elements, 3.3 % for 25-voxel elements, 3.4 % for 50-voxel elements, and 3.5 % for 100-voxel elements. As the number of kinematic degrees of freedom decreases (*i.e.*, the element size increases), the correlation residuals are expected to degrade. The fact that the degradation remains small is an indication that the correlation was globally successful, irrespective

of the discretization. These results were obtained for the first step. The same trends are observed for the second step, but with slightly higher levels, thereby indicating that the cracking activity has increased. The mean correlation residuals at convergence is equal to 3.3 % for 12-voxel elements, 3.5 % for 25-voxel elements, 3.6 % for 50-voxel elements, and 3.8 % for 100-voxel elements.

The standard deviation of the volume difference  $f - \tilde{g}$ , where  $\tilde{g}$  denotes the volume in the deformed configuration corrected by the measured displacement for the first step, is equal to 10.5 gray levels for 12-voxel elements, 11.0 gray levels for 25-voxel elements, 11.5 gray levels for 50-voxel elements, and 12.1 gray levels for 100-voxel elements. The same trend as before is observed. Had cracks not appeared, it would correspond to a noise level on the order of 7.4-8.6 gray levels (*i.e.*, not that far from the second noise level considered in the resolution analysis (*i.e.*, 6 gray levels, see Section 3.2). For the second step, the same trends are observed with standard deviations ranging from 10.7 to 13.5 gray level when the element size varies from 12 voxels to 100 voxels.

## 4.2 Damage mechanisms

The analysis of the correlation residuals enabled us to deem the correlation results globally trustworthy. Various causes can lead to higher correlation residuals, which call for attention. First, the whole registration may not be satisfactory. This is not the case as proven by Figures 4(c) and 5. Second, the gray level conservation may not be satisfied, possibly due to the reconstruction stage. However, Figures 4(c) and 5 do not indicate significant biases. Third, the kinematic hypotheses during correlation may no longer be fulfilled. For instance, when analyzing cracks, a C8 kinematic basis does not allow for displacement discontinuities. One solution is then to enrich the kinematic basis [32] as in the extended finite element method [33,34]. The correlation residuals are then used to determine the 0-contour level set associated with crack surface [21]. This

procedure will not be used herein. The analysis will be restricted to the correlation residuals and their change with time when C8-DVC is utilized.

To proceed, the first issue to solve is the element size to choose for the analysis of cracking. Figure 6 shows transverse cuts of the volume in the deformed configuration corrected by the measured displacement,  $\tilde{g}$ , for different discretizations. The underlying discretization is distinguishable in the maps in the vicinity of cracks. For 12-voxel elements, the kinematics and therefore the microstructural description is the finest so that the cracks are likely to be better captured (and closed since the displacement is better described). As the element size increases, the cracks become easier to pinpoint, however the spatial resolution of the kinematic description becomes poorer. In the sequel four different discretizations will be studied.

Figure 7 shows transverse cuts of the correlation residual at the same height (*i.e.*, 3/4 of the total height) for the two steps. The corresponding gray level map is also shown. When compared to the latter, the former proves once again that the registration was generally successful except at locations where cracks appear. Most of the cracks are present at the first step. Since the residual levels increase from the first step to the second, it can be assumed that the crack openings follow the same trend (*i.e.*, the residual level increases in some areas between step one and two), that new cracks have initiated and others have propagated.

Apart from the cracked zones, the underlying microstructure is no longer visible in the correlation residual maps corresponding to the two steps. This is another confirmation that the correlation was successful. It is also true for areas close to the cracks for which the kinematics is satisfactory. This result shows that the crack openings remain small and that the procedure proposed to analyze cracked samples with a continuous kinematics is feasible. The same type of procedure was applied to a propellant and led to the same conclusion [35].

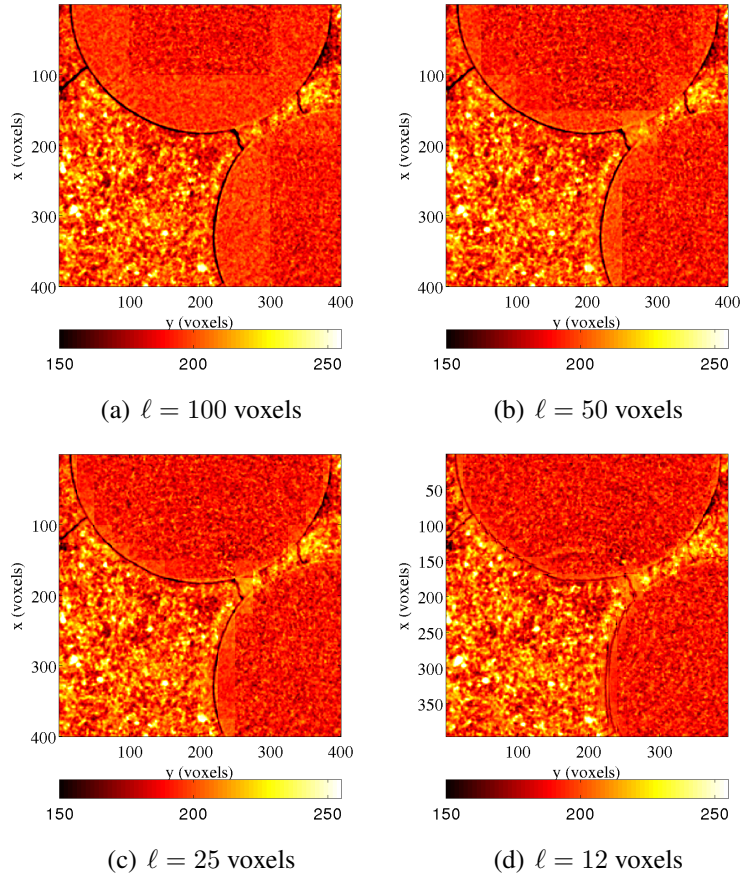


Figure 6: Cuts of the volume in the deformed configuration corrected by the measured displacement  $\tilde{g}$  for different element sizes for correlation analyses of the first step

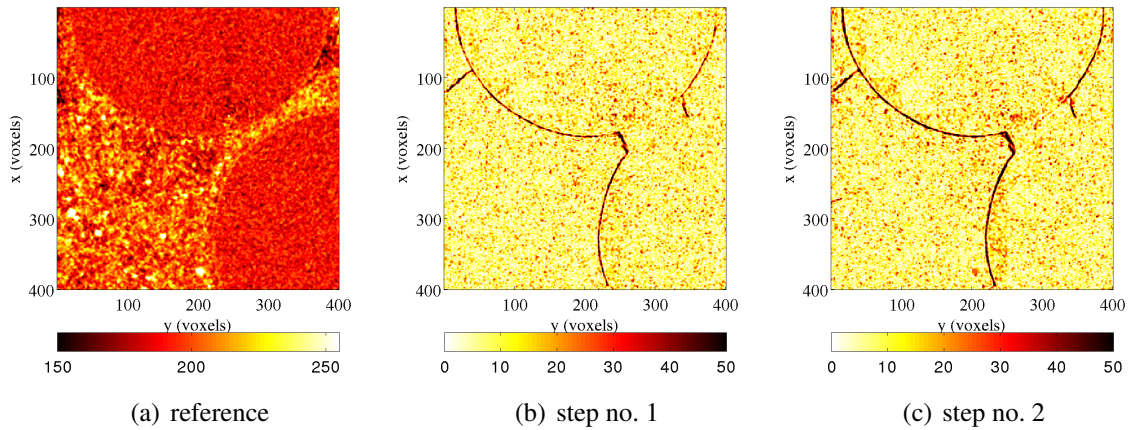


Figure 7: Correlation residuals for the two steps (b-c) and corresponding cut of the reference volume (a) when  $z = 300$  voxels. A C8-DVC analysis was run ( $\ell = 50$  voxels)

When analyzing Figures 6 and 7, it is concluded that two different mechanisms are active, namely, matrix cracking and inclu-

sion/matrix interfacial debonding. The former mechanism is less important in terms of surface fraction than the latter. When observing the 3D

rendering of the reference configuration (Figure 1), no cracks are visible. It can therefore be assumed that they were created during the two analyzed steps. Furthermore, most of the cracks were generated during the first step. Last, the cracking pattern can become very complex, and only the analysis of Figure 6 allows the two mechanisms to be clearly distinguished since the microstructure is also visible.

In DVC analyses, the first output is generally thought to be the measured displacement fields. They will be analyzed in the sequel. However, the correlation residuals were analyzed first. The reason for that is on the one hand to check

whether the registration was successful for both steps. A positive answer could be given. On the other hand, the small areas where the residuals are high allowed us to study the damage mechanisms and their development during the two steps. This was made possible thanks to voxel-based residuals, which are allowing for a voxel-scale description of the cracks.

### 4.3 Kinematic data

#### 4.3.1 Displacement field

The displacement field is shown for the first step.

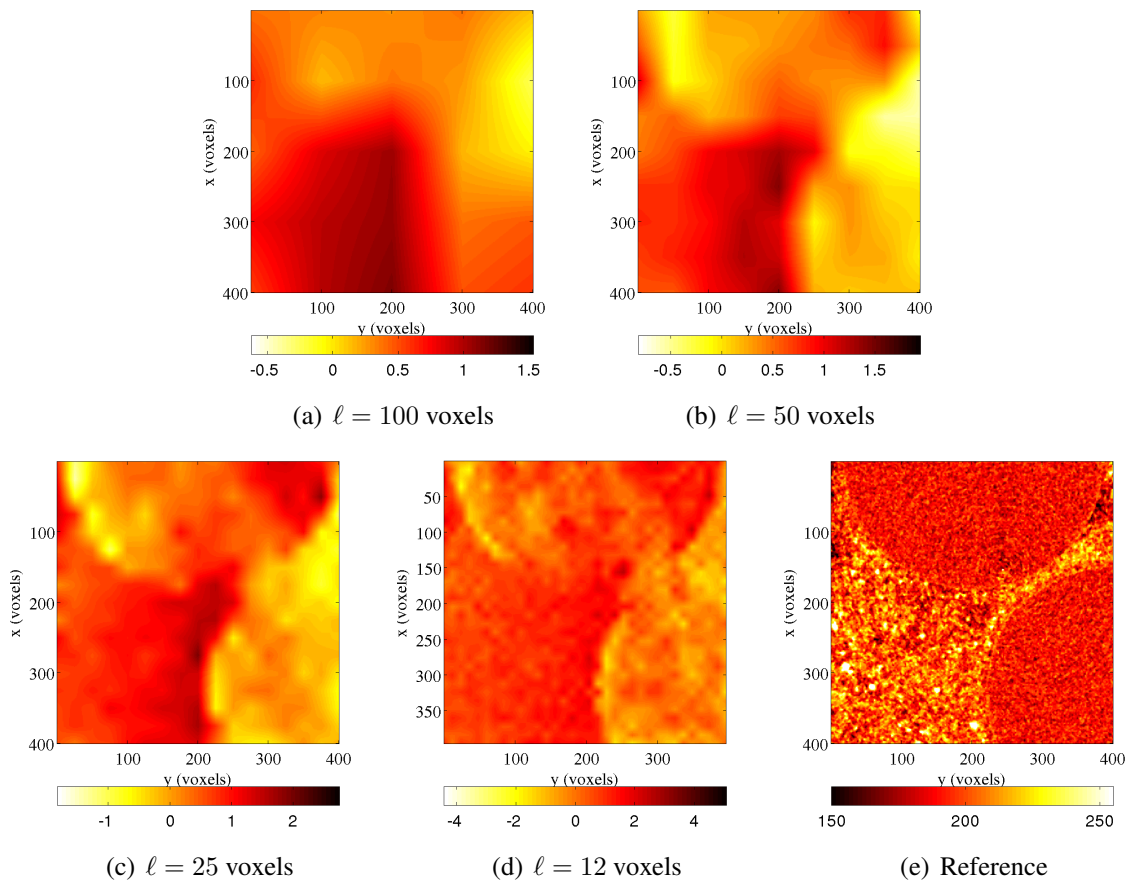


Figure 8: Displacement (expressed in voxels, 1 voxel  $\leftrightarrow$  5.1  $\mu\text{m}$ ) maps in the  $x$ -direction for different element sizes of correlation analyses of the first step. Corresponding cut of the reference volume (e) when  $z = 300$  voxels

Figure 8 shows displacement maps along the  $x$ -direction for different element sizes. When the discretization is coarse, the displacements are not well-described, as expected from higher

correlation residuals. This is true for the two drying steps. When compared to the underlying microstructure (Figure 8(e)), only the two finer discretizations are able to capture the com-

plex kinematics associated with the material microstructure and damage mechanisms.

In the following, strain data will be commented. It is worth remembering that different gauge lengths can be used to determine strains. Only one scale is considered, namely, for each C8 element (*i.e.*, mesoscopic scale), average values are computed.

### 4.3.2 Mesoscopic strains

The mesoscopic strains are computed from the mean displacement gradient per element. To analyze cracking, the mesoscopic maximum eigen strains are chosen. They are considered in the sequel when their value is positive (*i.e.*, indicating that cracking occurred) *and* greater than a threshold strain  $\epsilon_{th}$ , which is chosen to be three times the standard strain resolution (with a white Gaussian noise of standard deviation equal to  $6\sqrt{2}$  gray levels) so that most measurement uncertainties are avoided. Figure 9 shows the change of the mean value and its fluctuations (*i.e.*, error bars corresponding to the standard deviation). As the element size decreases, there is significant increase of both values. This result is again a proof that a fine discretization is needed in the present case, even though the

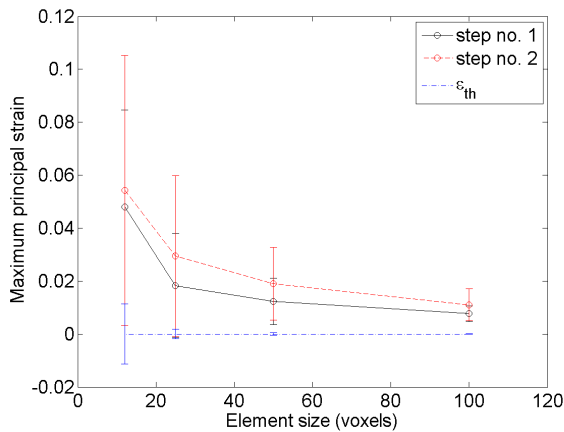


Figure 9: Average maximum principal strain for the two analyzed steps. The error bars indicate the standard deviation. Different discretizations are considered. The strain threshold  $\epsilon_{th}$  is defined as three times the standard strain resolution given by the resolution analysis (with a white noise of standard deviation equal to  $6\sqrt{2}$  gray levels)

strain resolution is higher. Since the level of  $\epsilon_{th}$  is significantly smaller than the fluctuations of the considered strains, for any chosen discretization. Most of the fluctuations are not due to measurement uncertainties but to cracking openings.

## 5 CONCLUSIONS

The development of relevant damage models is essential to understand and predict the mechanical behavior of concrete under drying and leaching [36]. To achieve this goal, micromechanical models can enlighten the complex interaction between cement paste and aggregates that produce microcracking [37], but the validation requires accurate measurements of the local (*i.e.*, micrometer scale) behavior. X-ray micro-tomography combined with Digital Volume Correlation (DVC) is a promising method that has been applied here on a sub sample of a simplified cementitious material in which the volume fraction of inclusions is high (*i.e.*, of the order of 35 %).

DVC is a powerful tool to analyze *ex situ* and *in situ* experiments in a tomograph (here the beamline was that of a third generation synchrotron). It yields 3D displacement fields in the bulk of the studied material. The strain resolution is sufficiently low to perform analyses of the studied material. Furthermore, the correlation residuals, which are usually utilized to assess the quality of the registration, were also used to analyze the damage mechanism seen as the main cause for non conservation of the gray levels since the kinematic basis was not consistent with the true one.

It was shown that debonding of the matrix/inclusion interfaces and matrix cracking are the two main damage mechanisms. These results correspond to a first step that showed the feasibility of DVC to analyze damage in cementitious composites. Next steps will be to analyze the full samples [36] and consider more realistic mortar compositions [38]. In terms of measurement procedures, two different paths may be followed to enrich the measured quantities. First, unstructured meshes may be used as was

proposed in 3D analyses of a propellant [39]. In the present case, the mesh topology should then be chosen in such a way that the interfaces between elements coincide with those between the inclusions and the matrix. One should remain cautious since small elements would then lead to higher measurement uncertainties as shown herein (Figure 3). A mechanical regularization may then allow to lower the displacement uncertainty [27]. Second, a voxel-scale discretization may also be considered. This approach always requires a mechanical regularization [27]. The main advantage though is that the discretization becomes the simplest to consider and the gray level may then be used, as shown herein, to regularize the volume registration. Both approaches will be assessed in the future.

## REFERENCES

- [1] Baruchel, J., Buffière, J.-Y., Maire, E., Merle, P. and Peix, G., 2000. *X-Ray Tomography in Material Sciences*. Hermes Science: Paris (France).
- [2] Weitkamp, T., Tafforeau, P., Boller, E., Cloetens, P., Valade, J.-P., Bernard, P., Peyrin, F., Ludwig, W., Helfen, L. and Baruchel, J., 2009. Status and evolution of the ESRF beamline ID19. *Proceedings ICXOM 2009*. AIP Conf. Proc.; 33-38.
- [3] *Industrial\_CT\_scanning*, September 2012. [en.wikipedia.org/wiki/Industrial\\_CT\\_scanning](http://en.wikipedia.org/wiki/Industrial_CT_scanning).
- [4] Buffière, J.-Y., Maire, E., Adrien, J., Masse, J.-P. and Boller, E., 2010. In Situ Experiments with X ray Tomography: an Attractive Tool for Experimental Mechanics. *Exp. Mech.* **50**(3):289-305.
- [5] Landis, E.N., Nagy, E.N. and Keane, D.T. 2003. Microstructure and fracture in three dimensions. *Eng. Fract. Mech.* **70**:911-925.
- [6] Garboczi, E.J., 2002. Three-dimensional mathematical analysis of particle shape using X-ray tomography and spherical harmonics: Application to aggregates used in concrete. *Cement Conc. Res.* **32**(10):1621-1638.
- [7] Wong, R.C.K. and Chau, K.T., 2005. Estimation of air void and aggregate spatial distributions in concrete under uniaxial compression using computer tomography scanning. *Cement Conc. Res.* **35**(8):1566-1576.
- [8] Garboczi, E.J. and Bullard, J.W., 2004. Shape analysis of a reference cement. *Cement Conc. Res.* **34**:1933-1937.
- [9] Gallucci, E., Scrivener, K., Groso, A., Stampanoni, M. and Margaritondo, G., 2007. 3D experimental investigation of the microstructure of cement pastes using synchrotron X-ray microtomography ( $\mu$ CT). *Cement Conc. Res.* **37**:360-368.
- [10] Promentilla, M.A.B., Sugiyama, T., Hitomi, T. and Takeda, N., 2009. Quantification of tortuosity in hardened cement pastes using synchrotron-based X-ray computed microtomography. *Cement Conc. Res.* **39**(6):548-557.
- [11] Bentz, D.P., Martys, N.S., Stutzman, P.E., Levenson, M.S., Garboczi, E.J., Dunsmuir, J. and Schwartz, L.M., 1995. X-Ray Microtomography of an ASTM C109 Mortar Exposed to Sulfate Attack. *Proceedings MRS Symposium*. MRS, Pittsburgh (PA), USA, 77-82.
- [12] Provis, J.L., Myers, R.J., White, C.E., Rose, V. and van Deventer, J.S.J., 2012. X-ray microtomography shows pore structure and tortuosity in alkali-activated binders. *Cement Conc. Res.* **42**(6):855-864.
- [13] Helfen, L., Dehn, F., Mikulík, P. and Baumbach, T., 2005. Three-dimensional imaging of cement microstructure evolution during hydration. *Adv. Cement Res.* **17**(3):103-111.

- [14] Burlion, N., Bernard, D. and Chen, D., 2006. X-ray microtomography: Application to microstructure analysis of a cementitious material during leaching process. *Cement Conc. Res.* **36**:346-357.
- [15] Rougelot, T., Burlion, N., Bernard, D. and Skoczylas, F., 2010. About microcracking due to leaching in cementitious composites: X-ray microtomography description and numerical approach. *Cement Conc. Res.* **40**(2):271-283.
- [16] Stock, S.R., Naik, N.K., Wilkinson, A.P. and Kurtis, K.E., 2002. X-ray microtomography (microCT) of the progression of sulfate attack of cement paste. *Cement Conc. Res.* **32**(10):1673-1675.
- [17] Naik, N.N., Jupe, A.C., Stock, S.R., Wilkinson, A.P., Lee, P.L. and Kurtis, K.E., 2006. Sulfate attack monitored by microCT and EDXRD: Influence of cement type, water-to-cement ratio, and aggregate. *Cement Conc. Res.* **36**(1):144-159.
- [18] Poinard, C., Piotrowska, E., Malecot, Y., Daudeville, L. and Landis, E.N., 2012. Compression triaxial behavior of concrete: The role of the mesostructure by analysis of xray tomographic images. *Eur. J. Envir. Civil Eng.* **16**:115-136.
- [19] Sutton, M.A., Orteu, J.-J. and Schreier, H., 2009. *Image correlation for shape, motion and deformation measurements: Basic Concepts, Theory and Applications*. Springer: New York, NY (USA).
- [20] Hild, F. and Roux, S., 2012. Digital Image Correlation. *Optical Methods for Solid Mechanics. A Full-Field Approach*, Hack, E. and Rastogi, P., eds. Wiley-VCH: Berlin (Germany); 183-228.
- [21] Rannou, J., Limodin, N., Réthoré, J., Gravouil, A., Ludwig, W., Baietto, M.-C., Buffière, J.-Y., Combescure, A., Hild, F. and Roux, S., 2010. Three dimensional experimental and numerical multi-scale analysis of a fatigue crack. *Comp. Meth. Appl. Mech. Eng.* **199**:1307-1325.
- [22] Roux, S., Hild, F., Viot, P. and Bernard, D., 2008. Three dimensional image correlation from X-Ray computed tomography of solid foam. *Comp. Part A* **39**(8):1253-1265.
- [23] Bay, B.K., Smith, T.S., Fyhrie, D.P. and Saad, M., 1999. Digital volume correlation: three-dimensional strain mapping using X-ray tomography. *Exp. Mech.* **39**:217-226.
- [24] Smith, T.S., Bay, B.K. and Rashid, M.M., 2002. Digital volume correlation including rotational degrees of freedom during minimization. *Exp. Mech.* **42**(3):272-278.
- [25] Bornert, M., Chaix, J.-M., Doumalin, P., Dupré, J.-C., Fournel, T., Jeulin, D., Maire, E., Moreaud, M. and Moulinec, H., 2004. Mesure tridimensionnelle de champs cinématiques par imagerie volumique pour l'analyse des matériaux et des structures. *Inst. Mes. Métrol.* **4**:43-88.
- [26] Verhulp, E., van Rietbergen, B. and Huiskes, R., 2004. A three-dimensional digital image correlation technique for strain measurements in microstructures. *J. Biomech.* **37**(9):1313-1320.
- [27] Leclerc, H., Périé, J.-N., Roux, S. and Hild, F., 2011. Voxel-scale digital volume correlation. *Exp. Mech.* **51**(4):479-490.
- [28] Leclerc, H., Périé, J.-N., Hild, F. and Roux S., 2012. Digital Volume Correlation: What are the limits to the spatial resolution? Submitted for publication.
- [29] Hild, F. and Roux, S., 2012. Comparison of local and global approaches to digital image correlation. *Exp. Mech.* 2012; in press, DOI 10.1007/s11340-012-9603-7.

- [30] Hild, F., Maire, E., Roux, S. and Witz, J.-F., 2009. Three dimensional analysis of a compression test on stone wool. *Acta Mat.* **57**:3310-3320.
- [31] Benoit, A., Guérard, S., Gillet, B., Guillot, G., Hild, F., Mitton, D., Périé, J.-N. and Roux, S., 2009. 3D analysis from micro-MRI during in situ compression on cancellous bone. *J. Biomech.* **42**:2381-2386.
- [32] Réthoré, J., Tinnes, J.-P., Roux, S., Buffière, J.-Y. and Hild, F., 2008. Extended three-dimensional digital image correlation (X3D-DIC). *C. R. Mécanique* **336**:643-649.
- [33] Black, T. and Belytschko, T., 1999. Elastic crack growth in finite elements with minimal remeshing. *Int. J. Num. Meth. Eng.* **45**:601-620.
- [34] Moës, N., Dolbow, J. and Belytschko, T., 1999. A finite element method for crack growth without remeshing. *Int. J. Num. Meth. Eng.* **46**(1):133-150.
- [35] Hild, F., Fanget, A., Adrien, J., Maire, E. and Roux, S., 2011. Three dimensional analysis of a tensile test on a propellant with digital volume correlation. *Arch. Mech.* **63**(5-6):1-20.
- [36] Rougelot, T., Peng, C., Burlion, N. and Bernard, D., 2010. Why is it necessary to use a damage model to simulate the mechanical behavior of concrete under drying and leaching. *Europ. J. Envir. Civil Eng.* **14**(6-7):923-935.
- [37] Rougelot, T., Burlion, N., Bernard, D. and Skoczylas, F., 2010. About microcracking due to leaching in cementitious composites: X-ray microtomography and numerical approach. *Cement Conc. Comp.* **40**:271-283.
- [38] Burlion, N., Bernard, D. and Chen, D., 2006. X-ray microtomography: application to microstructure analysis of a cementitious material during leaching process. *Cement Conc. Res.* **36**:346-357.
- [39] Besnard, G., Hild, F., Leclerc, H., Périé, J.-N., Roux, S. and Réthoré, J., 2010. La corrélation d'images : un outil de mécanique expérimentale. *Proc. Congrès National MECAMAT*, 16 p.